

Statistics of drops generated from ensembles of randomly corrugated ligaments

Sagar Pal,^{1,2} César Pairetti,^{1,3, a)} Marco Cialesi-Esposito,^{4,1} Daniel Fuster,^{1,2} and Stéphane Zaleski^{1,2,5}

¹⁾*Sorbonne Université, Institut Jean Le Rond d'Alembert, UMR 7190, Paris, France*

²⁾*Centre National de la Recherche Scientifique, UMR 7190, Paris, France*

³⁾*Universidad Nacional de Rosario, Rosario, Argentina*

⁴⁾*Department of Engineering 'Enzo Ferrari', University of Modena and Reggio Emilia, 41125 Modena, Italy*

⁵⁾*Institut Universitaire de France, Paris, France*

(Dated: 2 October 2024)

The size of drops generated by the capillary-driven disintegration of liquid ligaments plays a fundamental role in several important natural phenomena, ranging from heat and mass transfer at the ocean-atmosphere interface to pathogen transmission. The inherent non-linearity of the equations governing the ligament destabilization leads to significant differences in the resulting drop sizes, owing to small fluctuations in the myriad initial conditions. Previous experiments and simulations reveal a variety of drop size distributions, corresponding to competing underlying physical interpretations. Here, we perform numerical simulations of individual ligaments, the deterministic breakup of which is triggered by random initial surface corrugations. The simulations are grouped in a large ensemble, each corresponding to a random initial configuration. The resulting probability distributions reveal three stable drop sizes, generated via a sequence of two distinct stages of breakup. Four different distributions are tested, volume-based Poisson, Gaussian, Gamma and Log-Normal. Depending on the time, range of droplet sizes and criteria for success, each distribution has successes and failures. However the Log-Normal distribution roughly describes the data when fitting both the primary peak and the tail of the distribution while the number of droplets generated is the highest, while the Gamma and Log-Normal distributions perform equally well when fitting the tail. The study demonstrates a precisely controllable and reproducible framework, which can be employed to investigate the mechanisms responsible for the polydispersity of drop sizes found in complex fluid fragmentation scenarios.

^{a)}paire.cesar@gmail.com

I. INTRODUCTION

Liquid fragmentation is the transformation of a compact volume into drops. The simplest example is the capillary-driven breakup of a slender cylindrical structure¹ at approximately regular intervals driven via the growth of long wavelength perturbations^{2–4}. In more general atomization problems, the initial liquid mass deforms transitioning to sheets^{5,6}, where the inertial expansion opposed by the capillary deceleration of the edges results in the formation of liquid rims, the subsequent destabilization of which leads to drops. A similar process develops when a perforation occurs in the liquid sheets, then the rapid capillary-driven expansion of holes^{7,8} forms an interconnected set of filaments, which eventually break into drops. The evolution of these topological changes are also affected by shear stresses^{9,10}, introducing the effects of Kelvin-Helmholtz¹¹ instabilities that induce many of the aforementioned transitions. Given the turbulent regime for atomization, the evolution of liquid structures is chaotic and strongly dependent on initial conditions. The only common feature that unites these seemingly disparate fragmentation processes is that the topological stage leading to drop formation is constituted by cylindrical thread-like structures, called ligaments or filaments.

The size of drops resulting from the breakup of ligaments governs physical mechanisms underlying a broad range of natural processes and industrial applications. These processes include the exchange of heat and mass transfer at the ocean-atmosphere interface^{12,13}, mixing/separation in metallurgical applications^{14,15}, pesticide dispersal and irrigation in industrial agriculture^{16–18}, and ever so important, pathogen transmission driven by violent respiratory events^{19,20}, among many other examples. Therefore, the development of quantitative models geared towards statistical predictions of the size and velocity of drops has drawn considerable scientific interest²¹ over the recent decades.

Several experimental and numerical investigations of drop size statistics have led to the popularization of three distinct classes of probability density functions, namely the Log-normal, Gamma and Poisson distributions, as outlined in the review by Villiermaux²². In addition, distributions such as the Gaussian⁶, Weibull²³, Exponential²⁴ and Beta²⁵ have also received significant attention. Regarding the interpretation of the underlying physical mechanisms, the Log-normal model²⁶ implies a sequential cascade of breakups (analogous to the Kolmogorov²⁷ energy cascade in fluid turbulence), the Gamma family²⁸ considers the competing effects of fragmentation and cohesion, and the Poisson model²⁹ entails instantaneous and random splitting of a volume into smaller fragments.

These models have been used in a diverse range of fragmentation scenarios to varying degrees of predictive success, however, there is a general lack of consensus regarding their generalization. This is primarily due to the fact that the initial liquid structures follow markedly different dynamical trajectories towards drop formation, rendering certain models incompatible with the actual physical mechanism at play (refer to⁶ for a discussion).

A. Modes of ligament breakup

The topological change from the threadlike ligaments to the (approximately) spherical geometry of drops can proceed along different paths, depending on the relative importance of viscosity and surface tension, the aspect-ratio, and the strength of the initial perturbation^{30–33}. Extremely viscous ligaments are stable against capillary-driven disintegration³⁴. For intermediate viscosities, the ligament ruptures at several locations along its length primarily due to the Rayleigh-Plateau instability³². In low-viscosity regimes, the ligament might also fragment from one of its free ends, referred to as the end-pinching mode^{30,35}. Additionally, if the ligament is free at both ends and not slender enough (small aspect-ratios), the capillary retraction might dominate and contract the entire volume into a single drop³⁶. Thus, despite the richness of end-pinching dynamics and complete contraction, the resulting drop sizes are extensively documented and well described by robust scaling laws^{30,37}. This turns our attention solely towards the drops formed due to breakups along the ligament length.

The breakup mechanism of liquid threads into droplets is fundamentally self-similar^{38,39}, corresponding to finite-time singularities in the Navier-Stokes equations. This feature means that the pinching process itself is largely independent of the initial conditions of the ligament. However, the internal liquid dynamics within the ligament are highly sensitive to these initial conditions due to the inherent non-linearities in the governing equations. The distribution of liquid volumes just before the thread ruptures is directly related to the volumes of the resulting droplets. Consequently, precise quantitative control over the initial conditions of the ligament is crucial for understanding the polydispersity in the sizes of the droplets formed.

B. Our computational framework

In this context, the main goal of this study is the design and conception of “numerical” experiments, that lend themselves to accurate and repeatable specifications of the initial conditions of the ligaments in question. Generally in physical experiments, obtaining ligaments conforming *exactly* to a specified geometrical shape and velocity field is extremely challenging. Thus, one often has to employ *a posteriori* correlations between the observed dispersion in the final drop sizes and the “qualitative” descriptions of initial conditions. In contrast, our present numerical framework allows us to obtain reproducible drop size distributions, which are purely outcomes of the mathematical model (Navier Stokes with surface tension), subject to a chosen set of parameters, initial and boundary conditions. Furthermore, most of the reported drop size distributions in experiments incorporate significant uncertainties, owing to small sample sizes. In our case, we are able to precisely control the degree of uncertainty in our eventual distributions, as the rapid calculation times enables us to generate large statistical samples.

II. METHODOLOGY

A. Mathematical Model

We use the one-fluid formulation for our system of governing equations, thus solving the incompressible Navier-Stokes equations throughout the whole domain, including regions of variable density and viscosity which itself depend on the explicit location of the interface separating the two fluids⁴⁰. The interface is modeled as having an infinitesimal thickness at the macroscopic scales under consideration. The temporal evolution of the interface is tracked by using an advection equation for the phase-characteristic function, which is essentially a Heaviside function that distinguishes the individual phases. The density and viscosity at each spatial location are expressed as linear functions of the phase-characteristic function.

B. Numerical Methods

We use the free scientific computing toolbox Basilisk^{42–44}, which couples finite-volume discretization with adaptive octree meshes (see Fig. 1c) in order to solve our governing partial differential equations. The interface evolution is tracked using a Volume-of-Fluid (VOF) method^{45,46},

coupled with a robust and accurate implementation of height-function based interface curvature computation⁴⁷. The capillary forces are modeled as source terms in the Navier-Stokes equations using the continuum surface-force⁴⁸ (CSF) method.

In the present context of ligament destabilization, the trajectory of the system towards drop formation is governed by non-linear interactions between capillary waves, remnants of the internal flow, acceleration of the liquid into the surrounding medium, localized vorticity production at the interface, as well as viscous dissipation in the bulk. In order to accurately reproduce the aforementioned multiscale phenomena and ensure sufficient spatio-temporal resolution in the vicinity of breakups and coalescence, the dynamically adaptive octree meshes (Fig. 1c.) are absolutely essential in order to carry out computationally efficient simulations. The accuracy and performance of Basilisk has been well documented and extensively validated for a variety of complex interfacial flows such as breaking waves^{49–51}, bursting bubbles^{52,53}, drop splashes⁵⁴, amongst many others.

C. Computational Setup

We conduct direct numerical simulations of air-water systems consisting of slender ligaments with spatial periodicity along the ligament axis. We use an axisymmetric framework that excludes all azimuthal variations in the shape of the ligament and subsequently formed drops. Fig. 1b illustrates the schematic of the computational setup, where the domain is a square of side L . The bottom side of the box acts as the axis of symmetry for the corrugated ligament (detailed view in the inset of Fig. 1b), which has an unperturbed (mean) radius R . The radial profile $R(x)$ along the ligament axis can be written as $R(x) = R + \varepsilon(x)$, where $\varepsilon(x)$ is considered to be a perturbation following a normal distribution with a mean value of 0 and variance ε_0^2 . Periodic boundary conditions are imposed for the primary variables on the left and right faces of the domain. Symmetry boundary conditions are imposed on the bottom side, with the impenetrable free-slip condition applied to the top side.

1. Random Surface Generation

The random surfaces of our spatially periodic ligaments are generated using a white noise signal, which is produced by a robust random number generator⁵⁵. This signal is then filtered to retain only the longest $n_c = 25$ wavelengths, given that only these are relevant for hydrodynamic

instabilities. resulting in the final radial profile of the ligament with a variance of ε_0^2 . The surface profile of each individual ligament in the ensemble is uniquely determined by the seed of the random number generator⁵⁵. This method allows us to create an ensemble of ligaments with random but unique surface profiles by varying the seed values.

For infinitely long ligaments, only perturbations with wavelengths longer than the ligament circumference are unstable to the Rayleigh-Plateau type capillary instability^{2,3}. Due to the discrete nature of numerical simulations, we can initially excite only a finite number of discrete modes that lie within the unstable spectrum (see Fig. 1a). The number of these unstable discrete modes is proportional to the ligament aspect-ratio $\Lambda = L/W$ ($\Delta k \sim \pi/\Lambda$). In our simulations, we have 15 discrete unstable modes, including several close to the optimal Rayleigh-Plateau wavelength.

2. *Regime of Interest*

In order to isolate the influence of initial geometrical shape on the subsequent dynamics and drops formed, we exclude inertial forces (axial stretching rate) in our initial conditions. The mean radius R of the ligament is the characteristic length scale of the problem. As we are dealing with air-water systems (20 degrees Celsius), the density and viscosity ratios are given as $\rho_l/\rho_g \simeq 830$ and $\mu_l/\mu_g \simeq 45$ respectively. Thus, our system is characterized by the Ohnesorge number which is defined as

$$\text{Oh} = \mu / \sqrt{\rho \sigma R}. \quad (1)$$

The Ohnesorge number is simply the square-root of the ratio of the viscous-capillary length scale ($l_\mu = \mu^2/\rho\sigma$) with the characteristic length scale of the problem (R). Although the configuration initially has no kinetic energy, a part of the surface potential is immediately converted into liquid inertia as soon as the system is released from its static initial conditions. The geometrical shape of any individual ligament in our ensemble is characterized by a mean corrugation amplitude $\eta = \varepsilon_0/R$, and aspect-ratio $\Lambda = L/W$, where $W = 2R$ denotes the mean width of the ligament. The volume of the corrugated ligament per unit spatial period (L) is controlled by Λ , which also acts as the theoretical upper bound to the drop size. Additionally, we rescale physical time with the capillary time scale such that $T = t/t_\sigma$, where $t_\sigma = (\rho R^3/\sigma)^{-1/2}$. The material properties used in our adimensional parameters (ρ , μ) correspond to the liquid phase i.e. water. In the present study, we focus our attention on *weakly* perturbed ($\eta \simeq 0.08$) and sufficiently slender ligaments ($\Lambda \simeq 50$) with $\text{Oh} \simeq 10^{-2}$, which correspond to water ligaments of a diameter close

to a 100 microns, representing the dynamics of the experiments on^{6,33} within a relevant range of dimensionless parameters^{56,57}..

III. RESULTS

The process of drop formation via ligament breakup is deterministic, therefore it is completely characterized by the initial geometrical shape of the ligament. Stochasticity is introduced by creating an ensemble of such corrugated ligaments, where each individual case has a random and unique surface. The statistical properties of the corrugated shape are identical across all ligaments in the ensemble. This key step allows us to incorporate the effects of the myriad underlying processes that determine the exact ligament shape in realistic fragmentation scenarios, that too in a quantitatively precise and reproducible manner.

A. Statistics of Drop Formation

In Fig. 2a, we illustrate the different stages involved in the breakup of an individual ligament into drops, where the ligament is randomly selected from our ensemble of size 10000. Linear theory based on the Rayleigh breakup^{2,3} of infinitely long liquid cylinders in a quiescent medium predicts the initial destabilization phase (panels $T = 8, T = 9$ of Fig. 2a) proceeding via exponential growth of the different (unstable) discrete frequencies that constitute the initial surface perturbation. Beyond this linear growth phase, non-linearities rapidly kick in near the breakup zones^{1,58,59}, eventually resulting in the formation of “main” and significantly smaller “satellite” droplets, as observed in panels $T = 11, T = 12$ of Fig. 2a. In our study, we refer to this as the first stage of breakups (**S1**), where we find a set of “primary” and “satellite” drops (orange dashed box in Fig. 2a), along with a collection of strongly deformed elongated structures (purple dashed box in Fig. 2a) which themselves resemble small aspect-ratio ligaments. This stage is immediately followed by the second stage of breakups (**S2**), in which the elongated structures break down into smaller fragments, while the previously formed primary and satellite drops remain stable.

The number of drops in our ensemble is measured using *average drop count*, defined as the ratio between the total number of drops in the ensemble to the total length of the ligament ensemble, measured in critical wavelength ($\lambda_{RP} = 2\pi/k_{RP} \simeq 9R$), corresponding to the maximum growth rate of the viscous Rayleigh-Plateau instability^{2,3,41}. In Fig. 2c, we plot the temporal variation of

average drop count. The slope of the graph is determined by the competition between breakup and coalescence events, thus delineating the two distinct stages of breakup (**S1** and **S2**), as well as the dominance of coalescence events beyond $T = 14$, leading to a slow decrease in the number of drops.

Coming to the statistics of drop sizes, in Fig. 2b, we show the probability density functions (PDF) corresponding to drop size distributions as a function of time. The drop diameters are re-scaled by the initial width (W) of the ligaments. One can clearly observe the presence and persistence of three distinct peaks in the size distribution for all instants of time shown. These stable peaks correspond to drop sizes given by $D/W \simeq 0.6$ for the satellite drops, $D/W \simeq 1.9$ for the primary drops, and $D/W \simeq 2.3$ for what we refer to as “secondary” drops.

Assuming that drops are formed by encapsulating the volume of liquid contained within one optimal wavelength ($2\pi/k_{\text{RP}}$), we can compute the diameter D_{RP} as

$$\frac{\pi}{6}D_{\text{RP}}^3 = \frac{\pi}{4}W^2(2\pi/k_{\text{RP}}) \implies D_{\text{RP}}/W \simeq 1.89. \quad (2)$$

As we can observe in Fig. 2b, the statistical estimate of our primary drop size (values distributed around $D/W \simeq 1.9$) across time is in excellent agreement with the predictions (2) of linearized stability theory.

The typical size of satellite drops has a strong dependence on the initial conditions, as meticulously documented in the seminal work of Ashgriz & Mashayek⁶⁰ concerning the capillary breakup of jets. In that study, the authors report a monotonic decrease in the satellite drop size as one increases the initial perturbation strength (Fig. 12 in⁶⁰). At the limit of vanishing perturbation strength (matching our initial conditions), Ashgriz & Mashayek obtain a satellite drop size of $D/W \simeq 0.6$, which matches quite well with the statistical observations of our satellite drop size (Fig. 2b).

Immediately after the first set of breakups (**S1**), there are plenty of elongated structures with free ends (including our “secondary” drops), which might be subject to the end-pinching mechanism. Several numerical, experimental and scaling analyses in existing literature (Shulkes³⁰, Gordillo & Gekle³⁷, Wang & Bourouiba⁶) have established that the size of drops generated via the end-pinching mechanism are deterministically characterised by the width of the ligament of origin, given by a near constant value of $D/W \simeq 1.5$ (although with an extremely weak dependence on inertial stretching rate). Therefore, the absence of any peak in our drop size statistics (Fig. 2c)

after $T = 12$ (beyond **S1**) around the value $D/W \simeq 1.5$ is a striking observation, asserting that negligible breakups occur via the end-pinching mode. Further investigations must be conducted in order to establish the exact cause of this absence.

B. First Stage of Breakups (S1)

We take a closer look at the probability of the large drop sizes immediately after the first set of breakups. We start with a simple model for the ligament pinching-off at several locations, with the assumption of a small, uniform and independent probability of the ligament pinching-off in each small length element dx . Therefore the spacing ℓ between any two pinch-off locations (see Fig. 3a) follows an exponential probability distribution

$$P_1(\ell) = \zeta \exp(-\zeta \ell), \quad (3)$$

where ζ is the average number of pinch-offs occurring over a unit length. In other words the probability that the pinched-off length is between ℓ and $\ell + d\ell$ is $P_1(\ell)d\ell$. It is then easy to show⁶¹ that the number n of pinch-offs over a length x follows the Poisson distribution

$$P_P(n; x) = \frac{(\zeta x)^n}{n!} \exp(-\zeta x). \quad (4)$$

The volume of the drop formed by encapsulating the volume between two successive pinch-off locations separated by a distance ℓ is clearly $V = \pi W^2 \ell / 4$ and the diameter of a spherical droplet with that volume is $d = [(3/2)W^2 \ell]^{1/3}$. Using the change of variable relation for probability distributions $P_1(\ell)d\ell = P_d(d)dd$ we obtain the expression for the PDF of the diameters as

$$P_d(d) = P_1(\ell) \frac{d\ell}{dd} = \frac{2\zeta d^2}{W^2} \exp[-2\zeta d^3 / (3W^2)]. \quad (5)$$

Thus the diameter distribution is identical to a Poisson distribution with $n = 2$ and we refer to it as the “volume-weighted” Poisson distribution arising from an exponential distribution of pinch-off intervals. The pinch-off rate for our numerical experiment is determined by first observing the number of drops formed: 117,329 drops/10,000 ligaments ≈ 12 drops per ligament. Since the average number of pinch-offs is equal to *one more* than the average number of drops, we obtain $\zeta \simeq 0.13$ as there are 100 units of length per ligament. In Fig. 3b, we plot the PDF of the drop size distribution at $T = 12$, as well the volume-weighted exponential PDF using $\zeta = 0.13$ (no free parameters). We observe that the tail of the distribution matches the predictions of the

volume-weighted exponential model of Eq. (5) quite satisfactorily, even though it cannot capture the probabilities of the primary and satellite drops.

We observe that the tail of the distribution at $T = 12$ contains small peaks (see Fig. 2a at $T = 12$, Fig. 3b), which corresponds to some *typical* sizes of the elongated structures, and we seek a simplified model to predict the size of such drops. As demonstrated in Fig. 3a, each “elongated drop”, formed after the Poisson-like pinch-off events, is assumed to be a connected set of smaller *characteristic* volumes. We consider, following the V definition given between Eqs. (4) and (5), a characteristic volume $V_{\text{RP}} = \frac{\pi}{4}W^2(2\pi/k_{\text{RP}})$ to model any given elongated structure as composed of integer multiples of the volume encapsulated under optimal viscous Rayleigh-Plateau wavelength.

Thus, given $V_n = n \cdot V_{\text{RP}}$, the diameters corresponding to the peaks in the inset of Fig. 3b should simply vary as $D_n/W = A \cdot n^{1/3}$, where $A = D_{\text{RP}}/W$ is the Rayleigh-Plateau optimal drop size. In Fig. 3c, we plot the predictions of this simple model against the statistically observed values of the peaks present in the distribution tail at $T = 12$ (inset Fig. 3b). The close agreement of our model with the statistical observations strongly suggests that the volume of each of the elongated structures (sizes larger than the primary drops) is close to an integer multiple of the volume of the typical RP primary drop. The number of primary drop volumes within one elongated structure is determined by exponentially distributed pinch-offs along the ligament.

C. Second Stage of breakups (S2)

We now turn our attention towards the large ($D/W > 1.9$) “elongated” drops during the second stage of breakups. Considering these structures as small aspect-ratio ligaments, they can collapse into a single (or two) drop(s) via the capillary-driven retraction of both the ends, or break up into multiple drops along its length through a Rayleigh-Plateau type instability mechanism. Driessen et al.³² demonstrate using a combination of analytical arguments and numerical simulations, the existence of a critical aspect-ratio Λ_{cr} , below which, the structure is entirely stable against the Rayleigh-Plateau instability. This critical Λ_{cr} is determined by equating the time taken by the optimal Rayleigh-Plateau perturbation to grow to the ligament radius, with the time taken by the two ends to retract to half the ligament length. The expression for Λ_{cr} provided by Driessen et al.³², but adapted to our problem setup is given as

$$\frac{|\log(\eta')|}{t_{\sigma} \cdot \omega_{\text{max}}} + (6\Lambda_{\text{cr}})^{1/3} - \Lambda_{\text{cr}} = 0, \quad (6)$$

where, η' indicates the degree to which the surface of the ligament (elongated drop) is perturbed. The perturbation strength corresponding to our initial condition η acts as the lower bound to η' simply due to the fact that the perturbations grow as a function of time. The optimal growth rate ω_{\max} is a function of the Ohnesorge number, and is calculated from the dispersion relation obtained by Weber⁴¹ (Fig. 1a) for the capillary instability at the low Reynolds limit of the Navier-Stokes equations. Using a simple root-finding algorithm for the non-linear equation 6, with $\eta' = \eta$, we obtain the critical aspect-ratio value for our setup as $\Lambda_{\text{cr}} \simeq 11.5$, which is a slight overestimation due to the fact the our elongated structures are significantly more perturbed than η . Computing the equivalent diameter for the volume contained in a ligament of mean width W and aspect-ratio Λ_{cr} , we get $D_{\text{cr}}/W \simeq 2.5$.

Revisiting Fig. 2b, we observe that the number (or probability) of drops lying to the right of the D_{cr}/W mark (orange dashed line) decreases with time starting from $T = 12$ to $T = 16$. In addition, the “secondary” peak is the only one whose height does not decrease with time, rather, increases steadily with time. This observation can be explained by the continuous breakup of the elongated drops into smaller fragments, till they finally attain aspect-ratios just below the critical threshold $\Lambda_{\text{cr}} \simeq 11.5$, at which point they become immune to any further capillary instability. Looking at peak representing the “secondary” drops, we observe that they lie just below the critical threshold $D_{\text{cr}}/W \simeq 2.5$, therefore demonstrating a qualitative match between the statistical observations of our simulations and the predictions of the “Driessen model³²” (Eq. 6).

Finally, we study the drop size distributions immediately after the second stage of breakups **S2** at $T = 14$. In terms of candidate probability density functions for the large drop sizes, we use the three most popular choices in existing literature, namely, the Gaussian, Log-Normal and Gamma distributions (definitions in the Appendix).

In Fig. 4, we plot the best fits pertaining to the aforementioned candidate functions on a log-linear scale, within different ranges of interest (vertical dashed lines). The histogram bins are ensemble averaged, where the 95% confidence intervals are computed using a standard bootstrap re-sampling procedure (refer to the Appendix). Fig. 4a demonstrates that by including the peak representing the primary drops, the distribution is *roughly* described by a Log-Normal distribution, where significant differences from the Gaussian and Gamma fits mainly appearing near the tail ($D/W > 3$). Subsequently, in Fig. 4b we restrict our focus to the tail, therefor excluding the primary drop peak. We observe the Log-Normal and Gamma fits appears to describe the probabilities of large sizes with similar accuracy, better than the Gaussian. This last fit misses the error bars

near the tail, while the other two fall within range. It is important to note that the upper limit to the drop size is given by the volume of the entire ligament; for our considerably slender ligaments ($\Lambda \simeq 50$), the largest drop size is given by $D_{\max}/W \simeq 4.2$. Thus, even while having converged statistics, sufficiently large samples and robust error bars, there is a fundamental limitation when it comes to distinguishing between the curvatures of our exponential candidate functions near the tail region, simply as a consequence of the restricted range ($1.9 < D/W < 4.2$) of drop sizes.

IV. CONCLUSIONS & PERSPECTIVES

The fragmentation of liquid masses in high-speed flows, such as atomizing jets, breaking waves, explosions or liquid impacts, is of utmost practical importance, and of interest for the statistical study of flows. Although drop size distributions can be inferred from experiments, our high-fidelity numerical approach crucially provides the direct predictions of the mathematical model i.e. Navier-Stokes with surface tension. Here we explore this distribution for the simplified case of a liquid ligament, where the simplification allows us to obtain high-fidelity solutions for ensembles that are so large that the statistical error is smaller than in most experiments to date. Thus, this study constructs a solution to the distribution problem based directly on the conventionally accepted mathematical model, that too in a quantitatively precise, statistically robust and reproducible framework.

Our statistical distributions reveal three stable drop sizes, generated via a sequence of two distinct breakup stages. After the 1st stage, the probability of the large sizes are shown to follow a parameter-free volume-weighted Poisson distribution, but immediately after the second breakup stage, the large sizes are best described by a two-parameter Log-Normal distribution, although the Gamma distribution seems to be the best fit for the distribution tail. Finally, we also point out that due to the small range of drop sizes involved, it is inherently difficult to distinguish between the curvatures of different exponential curves.

Moving forward, we would like to find a quantitative explanation concerning the absence of the end-pinching drop formation mode in our observations. In addition, we would like to verify the consistency of our findings across a broad span of length scales corresponding to $10^{-4} < Oh < 1$. The essential next steps in our effort towards developing a higher fidelity picture of realistic fragmentation scenarios would involve incorporating additional layers of complexity on top of our simplified ligament model, such as a stretching flow, turbulent fluctuations in both liquid and gas

phases, as well as high shear rates at the interface.

ACKNOWLEDGMENTS

This work has benefited from access to the HPC resources of CINES under the allocations 2018- A0052B07760 and 2019 - A0072B07760, and the resources of TGCC under the project 2020225418 granted respectively by GENCI and PRACE and by the Flash Covid grant of HPC resources. Support by the ERC ADV grant TRUFLOW and by the Fondation de France for the ANR action Flash Covid is gratefully acknowledged. We thank Lydia Bourouiba for fruitful discussions regarding liquid fragmentation, Gareth McKinley for planting the seed of the idea, and Stéphane Popinet for the Basilisk platform.

Appendix

Our drop population \mathcal{P} at $T = 14$ has a size equal to 138,693. From \mathcal{P} we draw a random sample of size 10000, which we denote as S_1 . Repeating this sampling procedure (with replacement) 200 times, we create an ensemble of such samples $\mathcal{E}_j = \{\mathcal{S}_1, \dots, \mathcal{S}_{200}\}_j$. Histograms are generated for all samples in \mathcal{E}_j , given a fixed set of binning intervals. An ensemble averaged histogram for \mathcal{E}_j is obtained by computing the mean of the corresponding bin heights over all samples \mathcal{S}_i , which are plotted in Fig. 4 (blue points with error bars). The standard error on the ensemble averaged bin heights is computed using bootstrapping: (i) the ensembling procedure is repeated to construct 50 such ensembles ($\{\mathcal{E}_1, \dots, \mathcal{E}_{50}\}$), (ii) ensemble averaged histograms are computed for each \mathcal{E}_j as previously described, (iii) the standard deviation of the average bin heights across $\{\mathcal{E}_1, \dots, \mathcal{E}_{50}\}$ gives us the standard error. The error bars in Fig. 4 represents a range of 4 standard deviations i.e. 95% confidence intervals. The probability density functions are defined as

$$\begin{aligned} \text{Gaussian : } P(x; A, B) &= \frac{1}{B\sqrt{2\pi}} \exp \left[-\frac{1}{2} \left(\frac{x-A}{B} \right)^2 \right], \\ \text{Log-Normal : } P(x; A', B') &= \frac{1}{xB'\sqrt{2\pi}} \exp \left[-\frac{1}{2} \left(\frac{\log x - A'}{B'} \right)^2 \right], \\ \text{Gamma : } P(x; \alpha, \beta) &= \frac{\beta^\alpha}{\Gamma(\alpha)} x^{\alpha-1} \exp(-\beta x). \end{aligned}$$

REFERENCES

- ¹D. Rutland and G. Jameson, “A non-linear effect in the capillary instability of liquid jets,” *Journal of Fluid Mechanics* **46**, 267–271 (1971).
- ²L. Rayleigh, “On the capillary phenomena of jets,” *Proc. R. Soc. London* **29**, 71–97 (1879).
- ³L. Rayleigh, “On the stability, or instability, of certain fluid motions,” *Proceedings of the London Mathematical Society* **1**, 57–72 (1879).
- ⁴J. Plateau, “Recherches expérimentales et théorique sur les figures d’équilibre d’une masse liquide sans pesanteur.” *Mémoires de l’Académie Royale des Sciences, des Lettres et des Beaux-Arts de Belgique* **23**, 1–1 (1849).
- ⁵N. Bremond, C. Clanet, and E. Villermaux, “Atomization of undulating liquid sheets,” *Journal of Fluid Mechanics* **585**, 421–456 (2007).
- ⁶Y. Wang and L. Bourouiba, “Unsteady sheet fragmentation: droplet sizes and speeds,” *Journal of Fluid Mechanics* **848**, 946–967 (2018).
- ⁷L. Opfer, I. Roisman, J. Venzmer, M. Klostermann, and C. Tropea, “Droplet-air collision dynamics: Evolution of the film thickness,” *Physical Review E* **89**, 013023 (2014).
- ⁸N. Dombrowski and R. Fraser, “A photographic investigation into the disintegration of liquid sheets,” *Philosophical Transactions of the Royal Society of London. Series A, Mathematical and Physical Sciences* **247**, 101–130 (1954).
- ⁹J. C. Lasheras and E. Hopfinger, “Liquid jet instability and atomization in a coaxial gas stream,” *Annual review of fluid mechanics* **32**, 275–308 (2000).
- ¹⁰Y. Ling, D. Fuster, G. Tryggvason, and S. Zaleski, “A two-phase mixing layer between parallel gas and liquid streams: multiphase turbulence statistics and influence of interfacial instability,” *Journal of Fluid Mechanics* **859**, 268–307 (2019).
- ¹¹P. Drazin, “Kelvin–helmholtz instability of finite amplitude,” *Journal of Fluid Mechanics* **42**, 321–335 (1970).
- ¹²L. Deike, L. Lenain, and W. K. Melville, “Air entrainment by breaking waves,” *Geophysical Research Letters* **44**, 3779–3787 (2017).
- ¹³J. H. Seinfeld, S. N. Pandis, and K. Noone, “Atmospheric chemistry and physics: from air pollution to climate change,” *Physics Today* **51**, 88 (1998).
- ¹⁴S. Johansen and F. Boysan, “Fluid dynamics in bubble stirred ladles: Part ii. mathematical modeling,” *Metallurgical Transactions B* **19**, 755–764 (1988).

- ¹⁵A. J. Yule and J. J. Dunkley, *Atomization of melts: for powder production and spray deposition*, 11 (Oxford University Press, USA, 1994).
- ¹⁶S. Kooij, R. Sijs, M. M. Denn, E. Villermaux, and D. Bonn, “What determines the drop size in sprays?” *Physical Review X* **8**, 031019 (2018).
- ¹⁷C. Stainier, M.-F. Destain, B. Schiffrers, and F. Lebeau, “Droplet size spectra and drift effect of two phenmedipham formulations and four adjuvants mixtures,” *Crop protection* **25**, 1238–1243 (2006).
- ¹⁸G. Matthews, *Pesticide application methods* (John Wiley & Sons, 2008).
- ¹⁹L. Bourouiba, E. Dehandschoewercker, and J. W. Bush, “Violent expiratory events: on coughing and sneezing,” *Journal of Fluid Mechanics* **745**, 537–563 (2014).
- ²⁰L. Bourouiba, “Turbulent gas clouds and respiratory pathogen emissions: potential implications for reducing transmission of covid-19,” *Jama* **323**, 1837–1838 (2020).
- ²¹E. Villermaux, “Fragmentation versus cohesion,” *J. Fluid Mech* **898**, P1 (2020).
- ²²E. Villermaux, “Fragmentation,” *Annu. Rev. Fluid Mech.* **39**, 419–446 (2007).
- ²³Y. Liu, Y. Laiguang, Y. Weinong, and L. Feng, “On the size distribution of cloud droplets,” *Atmospheric research* **35**, 201–216 (1995).
- ²⁴P. L. Smith, “Raindrop size distributions: Exponential or gamma—does the difference matter?” *Journal of Applied Meteorology* **42**, 1031–1034 (2003).
- ²⁵R. D. Cohen, “Shattering of a liquid drop due to impact,” *Proceedings of the Royal Society of London. Series A: Mathematical and Physical Sciences* **435**, 483–503 (1991).
- ²⁶M. Gorokhovski and V. Saveliev, “Analyses of kolmogorov’s model of breakup and its application into lagrangian computation of liquid sprays under air-blast atomization,” *Physics of Fluids* **15**, 184–192 (2003).
- ²⁷A. N. Kolmogorov, “Equations of turbulent motion in an incompressible fluid,” in *Dokl. Akad. Nauk SSSR*, Vol. 30 (1941) pp. 299–303.
- ²⁸E. Villermaux, P. Marmottant, and J. Duplat, “Ligament-mediated spray formation,” *Physical review letters* **92**, 074501 (2004).
- ²⁹M. S. Longuet-Higgins, “The crushing of air cavities in a liquid,” *Proceedings of the Royal Society of London. Series A: Mathematical and Physical Sciences* **439**, 611–626 (1992).
- ³⁰R. Schulkes, “The contraction of liquid filaments,” *Journal of Fluid Mechanics* **309**, 277–300 (1996).

- ³¹P. K. Notz and O. A. Basaran, “Dynamics and breakup of a contracting liquid filament,” *Journal of Fluid Mechanics* **512**, 223 (2004).
- ³²T. Driessen, R. Jeurissen, H. Wijshoff, F. Toschi, and D. Lohse, “Stability of viscous long liquid filaments,” *Physics of fluids* **25**, 062109 (2013).
- ³³F. Wang, F. Contò, N. Naz, J. Castrejón-Pita, A. Castrejón-Pita, C. Bailey, W. Wang, J. Feng, and Y. Sui, “A fate-alternating transitional regime in contracting liquid filaments,” *Journal of Fluid Mechanics* **860**, 640–653 (2019).
- ³⁴A. A. Castrejon-Pita, J. Castrejón-Pita, and I. Hutchings, “Breakup of liquid filaments,” *Physical review letters* **108**, 074506 (2012).
- ³⁵H. A. Stone and L. G. Leal, “Relaxation and breakup of an initially extended drop in an otherwise quiescent fluid,” *Journal of Fluid Mechanics* **198**, 399–427 (1989).
- ³⁶H. A. Stone, B. Bentley, and L. Leal, “An experimental study of transient effects in the breakup of viscous drops,” *Journal of Fluid Mechanics* **173**, 131–158 (1986).
- ³⁷J. M. Gordillo and S. Gekle, “Generation and breakup of worthington jets after cavity collapse. part 2. tip breakup of stretched jets,” *Journal of fluid mechanics* **663**, 331–346 (2010).
- ³⁸J. Eggers and E. Villermaux, “Physics of liquid jets,” *Reports on progress in physics* **71**, 036601 (2008).
- ³⁹J. Eggers, “Theory of drop formation,” *Physics of Fluids* **7**, 941–953 (1995).
- ⁴⁰G. Tryggvason, R. Scardovelli, and S. Zaleski, *Direct numerical simulations of gas–liquid multiphase flows* (Cambridge University Press, 2011).
- ⁴¹C. Weber, “Disintegration of liquid jets,” *Z. Angew. Math. Mech.* **1**, 136–159 (1931).
- ⁴²S. Popinet, “Basilisk, a free-software program for the solution of partial differential equations on adaptive cartesian meshes (2018),” URL <http://basilisk.fr> **1**.
- ⁴³J. A. van Hooft, S. Popinet, C. C. van Heerwaarden, S. J. van der Linden, S. R. de Roode, and B. J. van de Wiel, “Towards adaptive grids for atmospheric boundary-layer simulations,” *Boundary-layer meteorology* **167**, 421–443 (2018).
- ⁴⁴S. Popinet, “A quadtree-adaptive multigrid solver for the serre–green–naghdi equations,” *Journal of Computational Physics* **302**, 336–358 (2015).
- ⁴⁵D. Gueyffier, J. Li, A. Nadim, R. Scardovelli, and S. Zaleski, “Volume-of-fluid interface tracking with smoothed surface stress methods for three-dimensional flows,” *Journal of Computational physics* **152**, 423–456 (1999).

- ⁴⁶S. Popinet, “Gerris: a tree-based adaptive solver for the incompressible euler equations in complex geometries,” *Journal of Computational Physics* **190**, 572–600 (2003).
- ⁴⁷S. Popinet, “An accurate adaptive solver for surface-tension-driven interfacial flows,” *Journal of Computational Physics* **228**, 5838–5866 (2009).
- ⁴⁸J. U. Brackbill, D. B. Kothe, and C. Zemach, “A continuum method for modeling surface tension,” *Journal of computational physics* **100**, 335–354 (1992).
- ⁴⁹L. Deike, S. Popinet, and W. Melville, “Capillary effects on wave breaking,” *Journal of Fluid Mechanics* **769**, 541–569 (2015).
- ⁵⁰L. Deike, W. K. Melville, and S. Popinet, “Air entrainment and bubble statistics in breaking waves,” *Journal of Fluid Mechanics* **801**, 91–129 (2016).
- ⁵¹W. Mostert and L. Deike, “Inertial energy dissipation in shallow-water breaking waves,” *Journal of Fluid Mechanics* **890** (2020).
- ⁵²L. Deike, E. Ghabache, G. Liger-Belair, A. K. Das, S. Zaleski, S. Popinet, and T. Séon, “Dynamics of jets produced by bursting bubbles,” *Physical Review Fluids* **3**, 013603 (2018).
- ⁵³A. Berny, L. Deike, T. Séon, and S. Popinet, “Role of all jet drops in mass transfer from bursting bubbles,” *Physical Review Fluids* **5**, 033605 (2020).
- ⁵⁴J. López-Herrera, S. Popinet, and A. Castrejón-Pita, “An adaptive solver for viscoelastic incompressible two-phase problems applied to the study of the splashing of weakly viscoelastic droplets,” *Journal of Non-Newtonian Fluid Mechanics* **264**, 144–158 (2019).
- ⁵⁵M. Matsumoto and T. Nishimura, “Mersenne twister: a 623-dimensionally equidistributed uniform pseudo-random number generator,” *ACM Transactions on Modeling and Computer Simulation (TOMACS)* **8**, 3–30 (1998).
- ⁵⁶S. Pal, *Investigation of complex liquid-gas interfacial flows: a numerical study using advanced Volume-of-Fluid methods*, Ph.D. thesis, Sorbonne Université (2020).
- ⁵⁷S. Zaleski, S. Pal, D. Fuster, and M. Cialesi-Esposito, “Droplet generation in ensembles of randomly corrugated ligaments,” in *International Conference on Liquid Atomization and Spray Systems (ICLASS)*, Vol. 1 (2021).
- ⁵⁸P. Vassallo and N. Ashgriz, “Satellite formation and merging in liquid jet breakup,” *Proceedings of the Royal Society of London. Series A: Mathematical and Physical Sciences* **433**, 269–286 (1991).
- ⁵⁹H. Lee, “Drop formation in a liquid jet,” *IBM Journal of Research and Development* **18**, 364–369 (1974).

⁶⁰N. Ashgriz and F. Mashayek, “Temporal analysis of capillary jet breakup,” *Journal of Fluid Mechanics* **291**, 163–190 (1995).

⁶¹R. D. Yates and D. J. Goodman, *Probability and stochastic processes: a friendly introduction for electrical and computer engineers* (John Wiley & Sons, 2014).

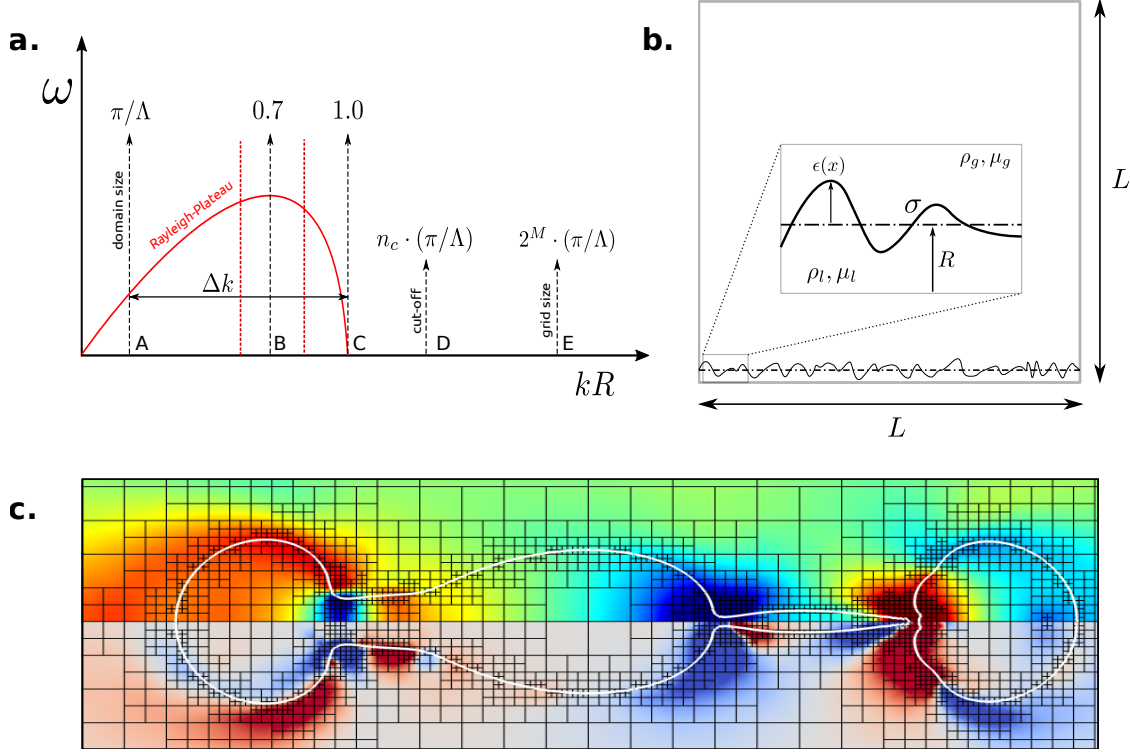


FIG. 1. **a.** Variation of the linearized growth rate (ω) corresponding to the viscous Rayleigh-Plateau (RP) instability as a function of nondimensional wavenumber kR^{41} . In our setup, n_c discrete wavelengths are excited as part of the initial condition, which fall within the vertical lines A and D. Only a certain number of these n_c discrete modes are unstable ($\omega > 0$) with respect to the RP instability (red curve, between vertical lines A and C). The vertical line B represents the approximate value of kR for which we get the optimal growth rate. **b.** Schematic of the computational setup. An infinitely long and axisymmetric corrugated ligament of mean radius R is placed along a side of a square domain of size L . The bottom side of the box acts as the axis of symmetry, while spatial periodicity is imposed along the horizontal direction. Inset : A close up view of the corrugated profile of the ligament, where the local radius is defined as the sum of the unperturbed (mean) radius R and the local perturbation $\epsilon(x)$. The material properties of the liquid and gas phases are denoted with the subscripts l and g respectively, which in our case corresponds to an air-water system with the surface tension coefficient σ . **c.** Dynamically adapted octree meshes near the interface, refined based on limiting second gradients of the volume fraction and velocity fields. The interface is represented by the white contours, the colormap on the top half is based on the axial velocity component, whereas the one on the bottom corresponds to that of vorticity. The colors red and blue correspond to the higher and lower end values respectively, in case of both colormaps.

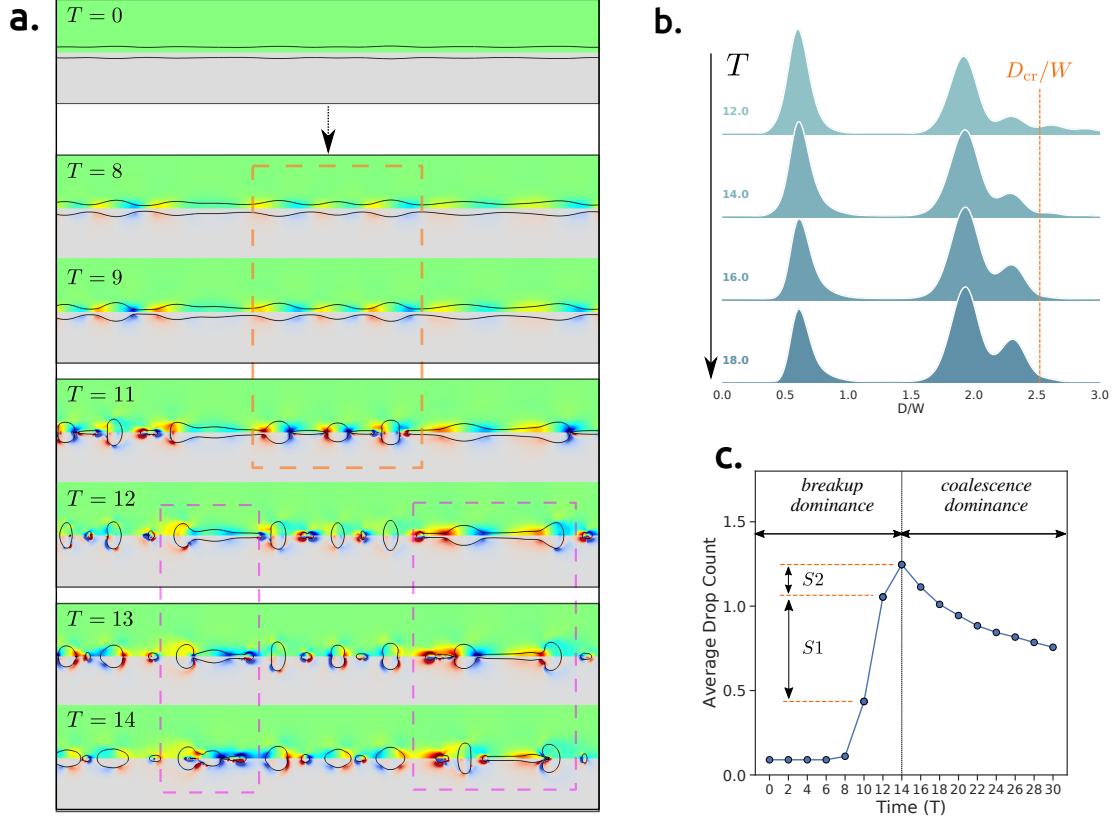


FIG. 2. **a.** Destabilization of a typical ligament through the breakup stages. The interface is represented by black contours. Colormaps of the top and bottom halves in each plot represent the axial velocity and the vorticity magnitude respectively. In snapshots $T = 8, 9, 11$, we observe the formation of drops (orange dashed box) corresponding to the optimally perturbed wavelength of the Rayleigh-Plateau instability. This leads to the first stage of breakups (**S1**), where the ligament disintegrates into primary, satellite and secondary drops, along with some elongated structures. The latter (purple dashed boxes), disintegrate into smaller sizes during the second stage of breakups (**S2**). **b.** Temporal evolution of the probability density functions of dimensionless drop size (D/W). Across time, the distribution peaks reveal three stable drop sizes, namely satellite ($D/W \simeq 0.6$), primary ($D/W \simeq 1.9$), and secondary ($D/W \simeq 2.3$) drops. The number of satellite drops decreases with time due to coalescence with adjacent larger drops. The number of primary and secondary drops increases with time due to the continuous breakup of the elongated structures with aspect-ratios above the critical threshold ($\Lambda_{cr}/W \sim (D_{cr}/W)^3$). **c.** The average number of drops in the ensemble as a function of time. Before $T = 6$, breakup is rare. Starting from $T = 8$, breakup events occurring on much faster timescales, leading to a peak in number of drops at $T = 14$. Beyond $T = 14$, coalescence dominates, leading to a slower decrease of the average drop count

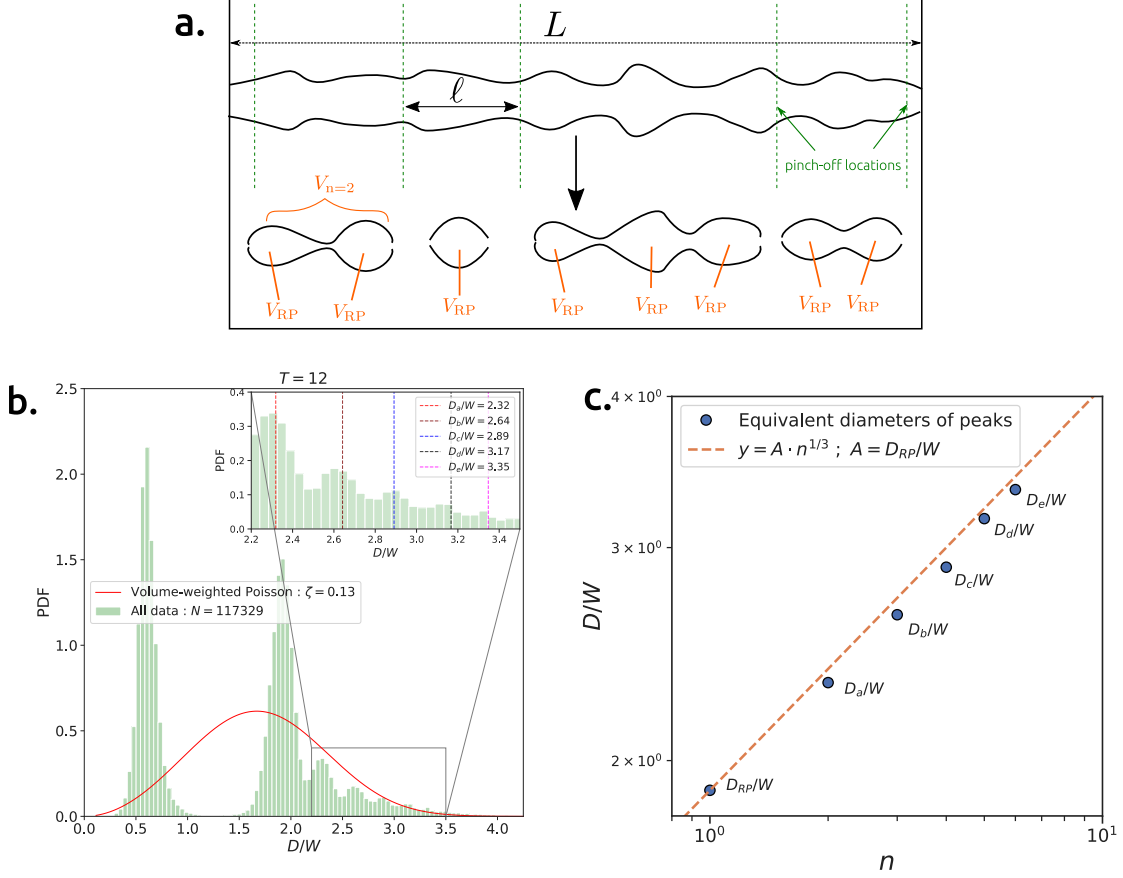


FIG. 3. **a.** Representation of the first stage of breakup dynamics (**S1**). The green vertical lines on the intact ligament (top figure) denote the possible pinch-off locations, spaced by an ℓ distance, along the length L of the ligament. After pinch-off, the volume V_n of the “elongated drops” can be modeled as multiple of V_{RP} , which corresponds to one unit of the optimally perturbed viscous Rayleigh-Plateau instability wavelength. **b.** Probability density function of the drop size at $T = 12$, displaying the peaks corresponding to the satellite and primary drops, as well as the typical sizes of the elongated drop-like structures in the distribution tail. The volume-weighted Poisson distribution (5) is plotted using a pinch-off rate ($\zeta = 0.13$) determined by the average number of drops formed per ligament. Inset: Zoom-up on the peaks representing the typical sizes of the elongated structures. **c.** The predictions of our simplified model (orange dashed line) for the typical sizes of the elongated structures, plotted alongside the statistical observations of the drop sizes (blue circles) that constitute the peaks within the tail of our distribution at $T = 12$. Assuming that the elongated structures are generated by encapsulating integer multiples of the characteristic volume V_{RP} , the equivalent diameters should scale according to $D_n/W \sim n^{1/3}$, where n is the number of characteristic units of V_{RP} .

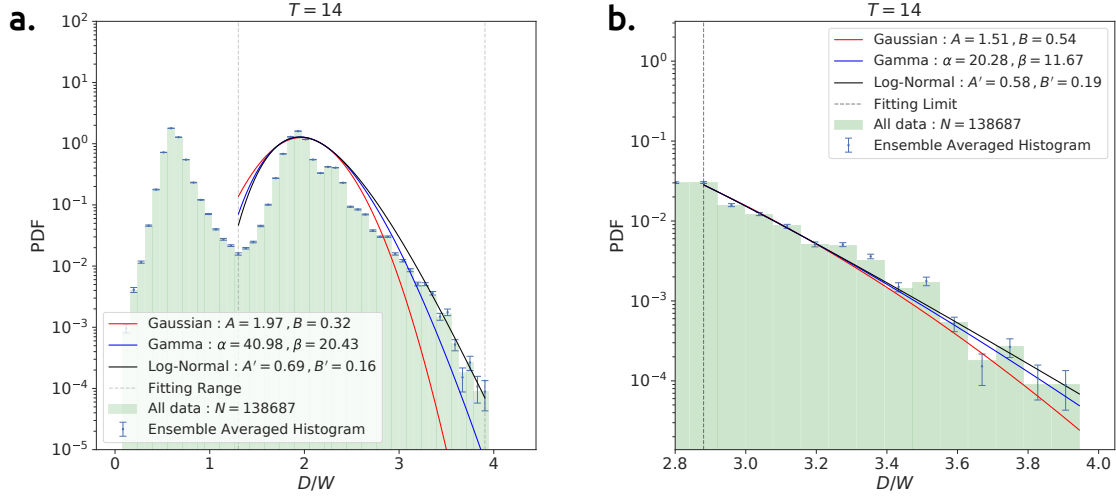


FIG. 4. Drop size distributions at $T = 14$, representing the drop ensemble immediately at the highest value of *average drop count*. Averaged distributions (blue points with error bars) with 95% confidence intervals are plotted on top of the distribution corresponding to the entire ensemble of size $N = 138,693$ (green histogram). **a.** The best fits corresponding to the Gaussian, Log-Normal and Gamma distribution functions are plotted within a range (dashed vertical lines) that *includes* the peak representing the primary drops. We observe that the Log-Normal fit best describes the distribution over the selected range, and differences comparing the Gamma fit appear only near the tail end of the distribution. **b.** The best fit corresponding to the Gaussian, Log-Normal and Gamma distribution are plotted while *excluding* the peak representing the primary drop size. For this range of sizes, Log-Normal and Gamma fits are still closer to the data, but it is difficult to distinguish between each of the three candidate functions.